An efficient and spectrally accurate numerical method for computing dynamics of rotating Bose–Einstein condensates

Weizhu Bao *, Hanquan Wang

Department of Mathematics, National University of Singapore, Singapore 117543, Singapore

Abstract

In this paper, we propose an efficient and spectrally accurate numerical method for computing the dynamics of rotating Bose–Einstein condensates (BEC) in two dimensions (2D) and 3D based on the Gross–Pitaevskii equation (GPE) with an angular momentum rotation term. By applying a time-splitting technique for decoupling the nonlinearity and properly using the alternating direction implicit (ADI) technique for the coupling in the angular momentum rotation term in the GPE, at every time step, the GPE in rotational frame is decoupled into a nonlinear ordinary differential equation (ODE) and two partial differential equations with constant coefficients. This allows us to develop new time-splitting spectral methods for computing the dynamics of BEC in a rotational frame. The new numerical method is explicit, unconditionally stable, and of spectral accuracy in space and second-order accuracy in time. Moreover, it is time reversible and time transverse invariant, and conserves the position density in the discretized level if the GPE does. Extensive numerical results are presented to confirm the above properties of the new numerical method for rotating BEC in 2D and 3D.
© 2006 Elsevier Inc. All rights reserved.

Keywords: Rotating Bose–Einstein condensates; Gross–Pitaevskii equation; Angular momentum rotation; Time spitting

1. Introduction

Since the first experimental creation of a quantized vortex in a gaseous Bose–Einstein condensate (BEC) [29,1,30,35], there has been significantly experimental and theoretical advances in the field of research [3,34,2,11,5,13,23,14,17,19,22]. Several experimental methods of vortex creation are currently in use, including phase imprinting [30,40], cooling of a rotating normal gas [24], and conversion of spin angular momentum into orbital angular momentum by reversal of the magnetic bias field in an Ioffe–Pritchard trap [26,27,33]. The topic of this paper is to propose an efficient and spectrally accurate numerical method for studying quantized vortex dynamics in a BEC by imposing a laser beam rotating with an angular velocity on the magnetic trap holding the atoms to create a harmonic anisotropic potential.

---

* Corresponding author. Tel.: +65 6874 3337; fax: +65 6774 6756.
  E-mail addresses: bao@cz3.nus.edu.sg (W. Bao), wanghanq@cz3.nus.edu.sg (H. Wang).
  URL: http://www.cz3.nus.edu.sg/~bao/ (W. Bao).

At temperatures T much smaller than the critical condensation temperature T_c, under mean field theory, the properties of a BEC in a rotational frame are modelled by the well-known time-dependent Gross–Pitaevskii equation (GPE) with an angular momentum rotation term [3,14,22]:

$$i\hbar\frac{\partial\psi(\mathbf{x},t)}{\partial t} = \left(-\frac{\hbar^2}{2m}\nabla^2 + V(\mathbf{x}) + NU_0|\psi|^2 - \Omega L_z\right)\psi(\mathbf{x},t), \quad \mathbf{x}\in\mathbb{R}^3, \ t\geqslant 0, \tag{1.1}$$

where $\mathbf{x}=(x,y,z)^{\mathrm{T}}$ is the Cartesian coordinate vector, $\psi(\mathbf{x},t)$ is the complex-valued macroscopic wave function, m is the atomic mass, $\hbar$ is the Planck constant, N is the number of atoms in the condensate, Ω is the angular velocity of rotating laser beam, $V(\mathbf{x})=\frac{m}{2}(\omega_x^2 x^2 + \omega_y^2 y^2 + \omega_z^2 z^2)$ with ω_x, ω_y and ω_z being the trap frequencies in x-, y- and z-directions, respectively. $U_0 = \frac{4\pi\hbar^2 a_s}{m}$ describes the interaction between atoms in the condensate with a_s the s-wave scattering length, and L_z is the z-component of the angular momentum. It is convenient to normalize the wave function by requiring

$$\|\psi(\cdot,t)\|^2 := \int_{\mathbb{R}^3} |\psi(\mathbf{x},t)|^2\,\mathrm{d}\mathbf{x} = 1. \tag{1.2}$$

After proper non-dimensionalization and dimension reduction, we can obtain the following dimensionless GPE with an angular momentum rotation term in the d-dimensions ($d = 2, 3$) [13,5,41]:

$$i\frac{\partial\psi(\mathbf{x},t)}{\partial t} = -\frac{1}{2}\nabla^2\psi + V_d(\mathbf{x})\psi + \beta_d|\psi|^2\psi - \Omega L_z\psi, \quad \mathbf{x}\in\mathbb{R}^d, \ t\geqslant 0, \tag{1.3}$$

$$\psi(\mathbf{x},0) = \psi_0(\mathbf{x}), \qquad \mathbf{x}\in\mathbb{R}^d \quad\text{with}\quad \|\psi_0\|^2 := \int_{\mathbb{R}^d}|\psi_0(\mathbf{x})|^2\,\mathrm{d}\mathbf{x} = 1, \tag{1.4}$$

where $L_z = -\mathrm{i}(x\partial_y - y\partial_x)$ and

$$V_d(\mathbf{x}) = \begin{cases} (\gamma_x^2 x^2 + \gamma_y^2 y^2)/2, & d = 2, \\ (\gamma_x^2 x^2 + \gamma_y^2 y^2 + \gamma_z^2 z^2)/2, & d = 3 \end{cases} \tag{1.5}$$

with γ_x, γ_y and γ_z being constants.

In order to study effectively the dynamics of BEC, especially in the strong repulsive interaction regime, i.e. $\beta_d \gg 1$ in (1.3), an efficient and accurate numerical method is one of the key issues. For non-rotating BEC, i.e. $\Omega = 0$ in (1.3), many efficient and spectrally accurate numerical methods were proposed in the literatures [7,6,11,4,12], and they were demonstrated that they are much better than the low-order finite difference methods [15,32,31,16]. Thus, they were applied to study collapse and explosion of BEC in 3D [8] and multi-component BEC [4] which are the very challenging problems in numerical simulation of BEC. Due to the appearance of the angular momentum rotation term in the GPE (1.3), new numerical difficulties are introduced. Currently, the numerical methods used in the physics literature for studying dynamics of rotating BEC remain limited [25,28,38,39], and they usually are low-order finite difference methods. Recently, some efficient and accurate numerical methods were designed for computing dynamics of rotating BEC. For example, Bao et al. [5] proposed a numerical method for computing dynamics of rotating BEC by applying a time-splitting technique for decoupling the nonlinearity in the GPE and adopting the polar coordinates or cylindrical coordinates so as to make the coefficient of the angular momentum rotation term constant. The method is time reversible, unconditionally stable, implicit but can be solved very efficiently, and conserves the total density. It is of spectral accuracy in transverse direction, but usually of second or fourth-order accuracy in radial direction. Another numerical method is the leap-frog spectral method used for studying vortex lattice dynamics in rotating BEC [41]. This method is explicit, time reversible, of spectral accuracy in space and second-order accuracy in time. But it has a stability constraint for time step [41]. The aim of this paper is to develop a numerical method which enjoys advantages of both the above two numerical methods. That is to say, the method is explicit, unconditionally stable, time reversible, time transverse invariant, and of spectral accuracy in space. We shall present such an efficient, unconditionally stable and accurate numerical method for discretizing the GPE in a rotational frame by applying a time-splitting technique and an ADI technique, and constructing appropriately spectral basis functions.

The paper is organized as follows. In Section 2, we review some properties of GPE in a rotational frame (1.3) including conservation laws and analytical solutions of condensate widths. In Section 3, we present a new time-splitting Fourier pseudospectral method for efficient and accurate simulation of GPE (1.3) in 2D and 3D. In Section 4, extensive numerical results are reported to demonstrate the efficiency and spectral resolution in space of our new numerical method. Finally, some conclusions are drawn in Section 5.

2. Some properties of the GPE

For the convenience of the reader, in this section, we will review some properties of the GPE with an angular momentum rotation term (1.3), which will be used to test our new numerical method proposed in the next section. First of all, the GPE (1.3) is time reversible and time transverse invariant. Second, it has at least two important invariants which are the *normalization of the wave function*

$$N(\psi) = \int_{\mathbb{R}^d} |\psi(\mathbf{x},t)|^2 \, d\mathbf{x} \equiv \int_{\mathbb{R}^d} |\psi(\mathbf{x},0)|^2 \, d\mathbf{x} = N(\psi_0) = 1, \quad t \geqslant 0, \tag{2.1}$$

and the *energy*

$$E_{\beta,\Omega}(\psi) = \int_{\mathbb{R}^d} \left[\frac{1}{2} |\nabla \psi|^2 + V_d(\mathbf{x})|\psi|^2 + \frac{\beta_d}{2} |\psi|^4 - \Omega \psi^* L_z \psi \right] d\mathbf{x} = E_{\beta_d,\Omega}(\psi_0), \quad t \geqslant 0, \tag{2.2}$$

where f^* and $\text{Im}(f)$ denote the conjugate and the imaginary part of the function f, respectively. Third, it was proven that at least for radial symmetric trap in 2D or cylindrical symmetric trap in 3D, i.e., $\gamma_x = \gamma_y$ in (1.3), the angular momentum expectation and energy for non-rotating part are conserved [5], that is, for any given initial data $\psi_0(\mathbf{x})$ in (1.4),

$$\langle L_z \rangle(t) \equiv \langle L_z \rangle(0), \qquad E_{\beta,0}(\psi) \equiv E_{\beta,0}(\psi_0), \quad t \geqslant 0, \tag{2.3}$$

where the angular momentum expectation which is a measure of the vortex flux is defined as

$$\langle L_z \rangle(t) := \int_{\mathbb{R}^d} \psi^*(\mathbf{x},t) L_z \psi(\mathbf{x},t) \, d\mathbf{x} = i \int_{\mathbb{R}^d} \psi^*(\mathbf{x},t)(y\partial_x - x\partial_y)\psi(\mathbf{x},t) \, d\mathbf{x}, \quad t \geqslant 0. \tag{2.4}$$

Other very useful quantities characterizing the dynamics of rotating BEC in 2D are the condensate width defined as

$$\delta_x(t) = \int_{\mathbb{R}^d} x^2 |\psi(\mathbf{x},t)|^2 \, d\mathbf{x}, \quad \delta_y(t) = \int_{\mathbb{R}^d} y^2 |\psi(\mathbf{x},t)|^2 \, d\mathbf{x}, \quad \delta_r(t) = \delta_x(t) + \delta_y(t). \tag{2.5}$$

As proven in [5], in 2D with a radial symmetric trap, i.e., $d = 2$ and $\gamma_x = \gamma_y := \gamma_r$ in (1.3), for any initial data $\psi_0(x,y)$ in (1.4), we have for any $t \geqslant 0$

$$\delta_r(t) = \frac{E_{\beta,\Omega}(\psi_0) + \Omega\langle L_z \rangle(0)}{\gamma_r^2} [1 - \cos(2\gamma_r t)] + \delta_r^{(0)} \cos(2\gamma_r t) + \frac{\delta_r^{(1)}}{2\gamma_r} \sin(2\gamma_r t), \tag{2.6}$$

where $\delta_r^{(0)} := \delta_r(0) = \delta_x(0) + \delta_y(0)$ and $\delta_r^{(1)} := \dot{\delta}_r(0) = \dot{\delta}_x(0) + \dot{\delta}_y(0)$ with for $\alpha = x$ or y

$$\delta_\alpha(0) = \delta_\alpha^{(0)} = \int_{\mathbb{R}^2} \alpha^2 |\psi_0(\mathbf{x})|^2 \, d\mathbf{x},$$

$$\dot{\delta}_\alpha(0) = \delta_\alpha^{(1)} = 2 \int_{\mathbb{R}^2} \alpha[-\Omega|\psi_0|^2(x\partial_y - y\partial_x)\alpha + \text{Im}(\psi_0^* \partial_\alpha \psi_0)] \, d\mathbf{x}.$$

Furthermore, when the initial data $\psi_0(x,y)$ in (1.4) satisfies

$$\psi_0(x,y) = f(r)e^{im\theta} \quad \text{with} \quad m \in \mathbb{Z} \quad \text{and} \quad f(0) = 0 \quad \text{when} \quad m \neq 0, \tag{2.7}$$

with (r, θ) being the polar coordinates in 2D, we have, for any $t \geqslant 0$,

$$\delta_x(t) = \delta_y(t) = \frac{1}{2}\delta_r(t) = \frac{E_{\beta,\Omega}(\psi_0) + m\Omega}{2\gamma_x^2} [1 - \cos(2\gamma_x t)] + \delta_x^{(0)} \cos(2\gamma_x t) + \frac{\delta_x^{(1)}}{2\gamma_x} \sin(2\gamma_x t). \tag{2.8}$$

These immediately imply that $\delta_r(t)$ is a periodic function with angular frequency doubling the trapping frequency in 2D with a radial symmetric trap, and also $\delta_x(t)$ and $\delta_y(t)$ are periodic functions with frequency doubling the trapping frequency provided that the initial data satisfies (2.7).

3. A time-splitting pseudospectral method for rotating BEC

In this section, we will present an explicit, unconditionally stable and spectrally accurate numerical method to solve the GPE (1.3) for dynamics of rotating BEC.

Due to the external trapping potential $V_d(\mathbf{x})$, the solution $\psi(\mathbf{x}, t)$ of (1.3) and (1.4) decays to zero exponentially fast when $|\mathbf{x}| \to \infty$. Thus in practical computation, we always truncate the problem (1.3) and (1.4) into a bounded computational domain with homogeneous Dirichlet boundary condition:

$$i\partial_t\psi(\mathbf{x}, t) = -\frac{1}{2}\nabla^2\psi + [V(\mathbf{x}) - iW(\mathbf{x})]\psi + \beta_d|\psi|^2\psi - \Omega L_z\psi, \quad \mathbf{x} \in \Omega_{\mathbf{x}}, \ t > 0, \tag{3.1}$$

$$\psi(\mathbf{x}, t) = 0, \quad \mathbf{x} \in \Gamma = \partial\Omega_{\mathbf{x}}, \ t \geqslant 0, \tag{3.2}$$

$$\psi(\mathbf{x}, 0) = \psi_0(\mathbf{x}), \quad \mathbf{x} \in \bar{\Omega}_{\mathbf{x}}, \tag{3.3}$$

where $W(\mathbf{x}) \geqslant 0$ corresponds to a localized loss term [36] and $V(\mathbf{x}) = V_d(\mathbf{x}) + V_p(\mathbf{x})$ with $V_p(\mathbf{x}) \geqslant 0$ a conservative repulsive pinning potential [36]. Here, we choose $\Omega_{\mathbf{x}} = [a, b] \times [c, d]$ in 2D, and resp., $\Omega_{\mathbf{x}} = [a, b] \times [c, d] \times [e, f]$ in 3D, with $|a|$, b, $|c|$, d, $|e|$ and f sufficiently large. The use of more sophisticated radiation boundary conditions is an interesting topic that remains to be examined in the future.

3.1. Time-splitting

We choose a time step size $\Delta t > 0$. For $n = 0, 1, 2, \ldots$, from time $t = t_n = n\Delta t$ to $t = t_{n+1} = t_n + \Delta t$, the GPE (3.1) is first solved in two splitting steps. One solves first

$$i\partial_t\psi(\mathbf{x}, t) = -\frac{1}{2}\nabla^2\psi(\mathbf{x}, t) - \Omega L_z\psi(\mathbf{x}, t) \tag{3.4}$$

for the time step of length Δt, followed by solving:

$$i\partial_t\psi(\mathbf{x}, t) = [V(\mathbf{x}) - iW(\mathbf{x})]\psi(\mathbf{x}, t) + \beta_d|\psi(\mathbf{x}, t)|^2\psi(\mathbf{x}, t), \tag{3.5}$$

for the same time step. For $t \in [t_n, t_{n+1}]$, multiplying (3.5) by ψ^*, the conjugate of ψ, we get

$$i\psi^*(\mathbf{x}, t)\partial_t\psi(\mathbf{x}, t) = [V(\mathbf{x}) - iW(\mathbf{x})]|\psi(\mathbf{x}, t)|^2 + \beta_d|\psi(\mathbf{x}, t)|^4. \tag{3.6}$$

Subtracting the conjugate of (3.6) from (3.6) and multiplying by $-i$, one obtains

$$\frac{\mathrm{d}}{\mathrm{d}t}|\psi(\mathbf{x}, t)|^2 = \psi^*\partial_t\psi + \psi\partial_t\psi^* = -2W(\mathbf{x})|\psi(\mathbf{x}, t)|^2. \tag{3.7}$$

Solving (3.7), we get

$$|\psi(\mathbf{x}, t)|^2 = e^{-2W(\mathbf{x})(t-t_n)}|\psi(\mathbf{x}, t_n)|^2, \quad t_n \leqslant t \leqslant t_{n+1}. \tag{3.8}$$

Substituting (3.8) into (3.5), we obtain

$$i\partial_t\psi(\mathbf{x}, t) = [V(\mathbf{x}) - iW(\mathbf{x})]\psi(\mathbf{x}, t) + \beta_d e^{-2W(\mathbf{x})(t-t_n)}|\psi(\mathbf{x}, t_n)|^2\psi(\mathbf{x}, t). \tag{3.9}$$

Integrate (3.9) from t_n to t, we find for $\mathbf{x} \in \Omega_{\mathbf{x}}$ and $t_n \leqslant t \leqslant t_{n+1}$:

$$\psi(\mathbf{x}, t) = \begin{cases} e^{-i[V(\mathbf{x}) + \beta_d|\psi(\mathbf{x},t_n)|^2](t-t_n)}\psi(\mathbf{x}, t_n), & W(\mathbf{x}) = 0, \\ \frac{\psi(\mathbf{x},t_n)}{e^{W(\mathbf{x})(t-t_n)}} e^{-i[V(\mathbf{x})(t-t_n) + \beta_d|\psi(\mathbf{x},t_n)|^2(1-e^{-2W(\mathbf{x})(t-t_n)})/2W(\mathbf{x})]}, & W(\mathbf{x}) > 0. \end{cases} \tag{3.10}$$

To discretize (3.4) in space, compared with non-rotating BEC [7,11,6], i.e. $\Omega = 0$ in (1.3), the main difficulty is that the coefficients in L_z are *not* constants which cause big trouble in applying sine or Fourier pseudospectral discretization. Due to the special structure in the angular momentum rotation term L_z (1.5), we will apply the

alternating direction implicit (ADI) technique and decouple the operator $-\frac{1}{2}\nabla^2 - \Omega L_z$ into two one dimensional operators such that each operator becomes a summation of terms with constant coefficients in that dimension. Therefore, they can be discretized in space by Fourier pseudospectral method and the ODEs in phase space can be integrated analytically. The details for discretizing (3.4) in 2D and 3D will be presented in the next two subsections, respectively.

3.2. Discretization in 2D

When $d = 2$ in (3.4), we choose mesh sizes $\Delta x > 0$ and $\Delta y > 0$ with $\Delta x = (b - a)/M$ and $\Delta y = (d - c)/N$ for M and N even positive integers, and let the grid points be

$$x_j = a + j\Delta x, \quad j = 0, 1, 2, \ldots, M; \quad y_k = c + k\Delta y, \quad k = 0, 1, 2, \ldots, N.$$

Let ψ_{jk}^n be the approximation of $\psi(x_j, y_k, t_n)$ and ψ^n be the solution vector with component ψ_{jk}^n.

From time $t = t_n$ to $t = t_{n+1}$, we solve (3.4) first

$$i\partial_t \psi(\mathbf{x}, t) = -\frac{1}{2}\partial_{xx}\psi(\mathbf{x}, t) - i\Omega y \partial_x \psi(\mathbf{x}, t), \tag{3.11}$$

for the time step of length Δt, followed by solving:

$$i\partial_t \psi(\mathbf{x}, t) = -\frac{1}{2}\partial_{yy}\psi(\mathbf{x}, t) + i\Omega x \partial_y \psi(\mathbf{x}, t), \tag{3.12}$$

for the same time step. The detailed discretizations of (3.11) and (3.12) are shown in Appendix A.

3.3. Discretization in 3D

When $d = 3$ in (3.4), we choose mesh sizes $\Delta x > 0$, $\Delta y > 0$ and $\Delta z > 0$ with $\Delta x = (b - a)/M$, $\Delta y = (d - c)/N$ and $\Delta z = (f - e)/L$ for M, N and L even positive integers, and let the grid points be

$$x_j = a + j\Delta x, \quad 0 \leqslant j \leqslant M; \quad y_k = c + k\Delta y, \quad 0 \leqslant k \leqslant N; \quad z_l = e + l\Delta z, \quad 0 \leqslant l \leqslant L.$$

Let ψ_{jkl}^n be the approximation of $\psi(x_j, y_k, z_l, t_n)$ and ψ^n be the solution vector with component ψ_{jkl}^n.

Similar as those for 2D case, from time $t = t_n$ to $t = t_{n+1}$, we solve (3.4) first

$$i\partial_t \psi(\mathbf{x}, t) = \left(-\frac{1}{2}\partial_{xx} - \frac{1}{4}\partial_{zz} - i\Omega y \partial_x\right)\psi(\mathbf{x}, t), \tag{3.13}$$

for the time step of length Δt, followed by solving:

$$i\partial_t \psi(\mathbf{x}, t) = \left(-\frac{1}{2}\partial_{yy} - \frac{1}{4}\partial_{zz} + i\Omega x \partial_y\right)\psi(\mathbf{x}, t), \tag{3.14}$$

for the same time step. The detailed discretizations of (3.13) and (3.14) are shown in Appendix B.

3.4. Stability

We define the usual discrete l^2-norm for the solution ψ^n as

$$\|\psi^n\|_{l^2} = \sqrt{\frac{b - a}{M}\frac{d - c}{N}\sum_{j=0}^{M-1}\sum_{k=0}^{N-1}|\psi_{jk}^n|^2}, \tag{3.15}$$

for $d = 2$, and for $d = 3$

$$\|\psi^n\|_{l^2} = \sqrt{\frac{b - a}{M}\frac{d - c}{N}\frac{f - e}{L}\sum_{j=0}^{M-1}\sum_{k=0}^{N-1}\sum_{l=0}^{L-1}|\psi_{jkl}^n|^2}. \tag{3.16}$$

For the *stability* of the time-splitting spectral approximations (A.7) for 2D and (B.1) for 3D, we have the following lemma, which shows that the total density is conserved when $W(\mathbf{x}) \equiv 0$, and resp. decreased when $W(\mathbf{x}) > 0$, in the discretized level.

Lemma 3.1. *The time-splitting spectral schemes* (A.7) *for* 2*D and* (B.1) *for* 3*D GPE with an angular momentum rotation term are unconditionally stable. In fact, for any mesh sizes* $\Delta x > 0$, $\Delta y > 0$ *and* $\Delta z > 0$, *and time step size* $\Delta t > 0$,

$$\|\psi^n\|_{l^2} \leqslant \|\psi^{n-1}\|_{l^2} \leqslant \|\psi^0\|_{l^2} = \|\psi_0\|_{l^2}, \quad n = 1, 2, \ldots. \tag{3.17}$$

In addition, if $W(\mathbf{x}) \equiv 0$ *in* (3.1), *then we have*

$$\|\psi^n\|_{l^2} \equiv \|\psi^0\|_{l^2} = \|\psi_0\|_{l^2}, \quad n = 1, 2, \ldots. \tag{3.18}$$

Proof. Follows the line of the analogous results for the linear and nonlinear Schrödinger equations in [6,9,10, 7,12]. □

4. Numerical results

In this section, we first test the accuracy of our new numerical method (A.7) for 2D and (B.1) for 3D and compare our numerical results with the analytical results reviewed in Section 2. Then we apply our new numerical method to study vortex lattice dynamics in rotating BEC by changing the trapping frequencies and to generate a giant vortex by introducing a localized loss term. Our aim is not to find new physics phenomena but to demonstrate the efficiency and high resolution of our new numerical method.

4.1. Accuracy test

To test the accuracy of our numerical method in 2D, we take $\Omega = 0.7$ in (1.3). The initial condition in (1.4) is taken as

$$\psi_0(x, y) = \frac{(\gamma_x \gamma_y)^{\frac{1}{4}}}{\pi^{\frac{1}{2}}} e^{-(\gamma_x x^2 + \gamma_y y^2)/2}, \quad \mathbf{x} = (x, y)^{\mathrm{T}} \in \mathbb{R}^2. \tag{4.1}$$

We take $\gamma_x = 1.0$ and $\gamma_y = 2.0$ in (1.3) and (4.1). Similar example was used in [5,41] for testing numerical accuracy of different numerical methods for rotating BEC. The GPE (1.3) is solved on $[-8, 8] \times [-8, 8]$, i.e. we take $a = -8$, $b = 8$, $c = -8$ and $d = 8$. Let ψ be the *exact* solution which is obtained numerically by using our method with a very fine mesh and small time step, e.g. $\Delta x = \Delta y = \frac{1}{64}$ and $\Delta t = 0.0001$, and $\psi^{(\Delta x, \Delta y, \Delta t)}$ be the numerical solution obtained with the mesh size $(\Delta x, \Delta y)$ and time step Δt.

First, we test the spectral accuracy in space by choosing a very small time step $\Delta t = 0.0001$, and solving the problem for each fixed β_2 with different mesh size $\Delta x = \Delta y$ so that the discretization errors in time can be neglected comparing to those in space. The errors $\|\psi(t) - \psi^{(\Delta x, \Delta y, \Delta t)}(t)\|_{l^2}$ at $t = 0.5$ are shown in Table 1 for different values β_2 and $h = \Delta x = \Delta y$.

Next, we test the second-order accuracy in time. Table 2 lists the errors at $t = 0.5$ for different values of β_2 and time steps Δt with a fine mesh in space, i.e. $\Delta x = \Delta y = 1/16$.

Similarly, to test the accuracy of our numerical method in 3D, we take $\Omega = 0.7$ in (1.3). The initial condition in (1.4) is taken as

Table 1
Spatial discretization errors $\|\psi(t) - \psi^{(\Delta x, \Delta y, \Delta t)}(t)\|_{l^2}$ at $t = 0.5$ in 2D

h	1/2	1/4	1/8
$\beta_2 = 20$	2.68E−2	6.5E−5	3.41E−10
$\beta_2 = 50$	0.1315	2.01E−3	5.91E−8
$\beta_2 = 100$	0.4287	1.94E−2	8.89E−6

Table 2
Temporal discretization errors $\|\psi(t) - \psi^{(\Delta x, \Delta y, \Delta t)}(t)\|_{l^2}$ at $t = 0.5$ in 2D

Δt	1/40	1/80	1/160	1/320	1/640
$\beta_2 = 20$	7.86E−4	1.95E−4	4.86E−5	1.21E−5	3.02E−6
$\beta_2 = 50$	2.95E−3	7.24E−4	1.80E−4	4.49E−5	1.12E−5
$\beta_2 = 100$	7.98E−3	1.98E−3	4.76E−4	1.19E−4	2.96E−5

$$\psi_0(x, y, z) = \frac{(\gamma_x \gamma_y \gamma_z)^{\frac{1}{4}}}{\pi^{\frac{3}{4}} 2} e^{-(\gamma_x x^2 + \gamma_y y^2 + \gamma_y z^2)/2}, \quad \mathbf{x} = (x, y, z)^{\mathrm{T}} \in \mathbb{R}^3. \tag{4.2}$$

We take $\gamma_x = \gamma_y = \gamma_z = 1.0$ in (1.3) and (4.2), and solve the GPE (1.3) in 3D on $[-8, 8] \times [-8, 8] \times [-8, 8]$. Again let ψ be the *exact* solution which is obtained numerically by using our method with a fine mesh and small time step, e.g. $\Delta x = \Delta y = \Delta z = \frac{1}{8}$ and $\Delta t = 0.0001$, and $\psi^{(\Delta x, \Delta y, \Delta z, \Delta t)}$ be the numerical solution obtained with mesh size $(\Delta x, \Delta y, \Delta z)$ and time step Δt. Table 3 shows the spatial discretization errors $\|\psi(t) - \psi^{(\Delta x, \Delta y, \Delta z, \Delta t)}(t)\|_{l^2}$ at $t = 0.5$ with $\Delta t = 0.0001$ for different values β_3 and mesh sizes $h = \Delta x = \Delta y = \Delta z$. Table 4 lists the errors at $t = 0.5$ for different values of β_3 and time steps Δt with a fine mesh in space, i.e. $\Delta x = \Delta y = \Delta z = 1/8$.

From Tables 1–4, we can draw the following conclusions: (i) The method (A.7) or (B.1) is of spectral accuracy in space and second-order accuracy in time. (ii) For a given fixed mesh size and time step, when β_d is increasing, the errors are increasing too. This implies that when the number of atoms in the condensate is increasing, i.e. β_d is increasing, more grid points and smaller time step are needed in practical computation in order to achieve a given accuracy.

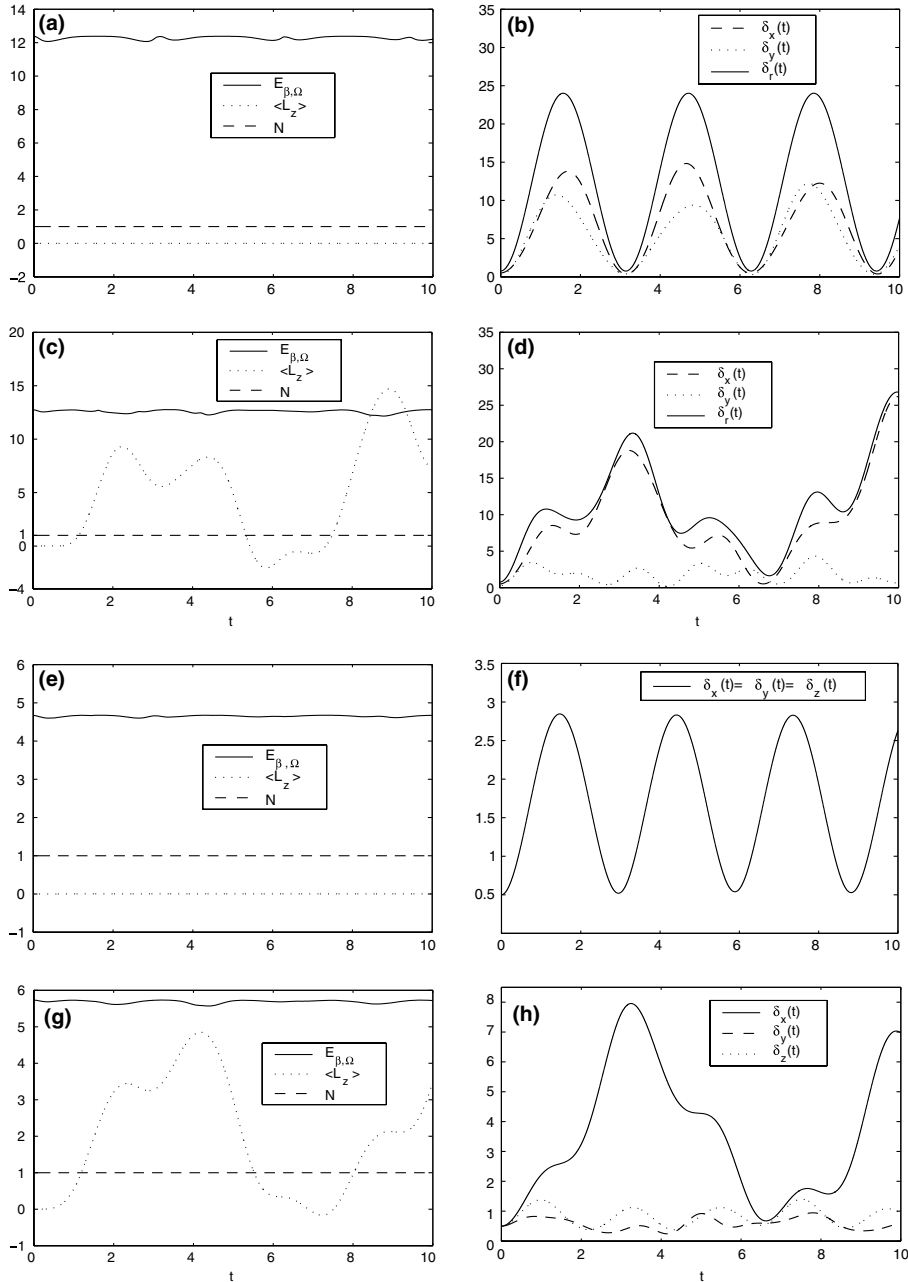Furthermore, Fig. 1 shows time evolution of the normalization $N(\psi)(t)$, energy $E_{\beta,\Omega}(\psi)(t)$, angular momentum expectation $\langle L_z \rangle(t)$ and condensate widths for the above parameters setup in 2D and 3D.

From Fig. 1, we can see that: (i) The normalization is conserved in both cases which confirms (2.1). (ii) The energy is not conserved in the discretized level, but the perturbation is very small, e.g. less than 5% (cf. (a), (c), (e) and (g) of Fig. 1). (iii) The angular momentum expectation is conserved when $\gamma_x = \gamma_y = 1$ (cf. (a) and (e) of Fig. 1) which confirms the analytical result (2.3), and oscillates when $1 = \gamma_x \neq \gamma_y = 2$ (cf. (c) and (g) of Fig. 1). (iv) The condensate widths $\delta_x(t)$, $\delta_y(t)$ and $\delta_r(t)$ are periodic functions when $\gamma_x = \gamma_y = 1$ which confirm the analytical result (2.6) (cf. (b) of Fig. 1), and are not periodic functions when $1 = \gamma_x \neq \gamma_y = 2$ (cf. (d) and (h) of Fig. 1).

4.2. Dynamics of a vortex lattice in rotating BEC

In this subsection, we numerically study the dynamics of a vortex lattice in rotating BEC by changing trap frequencies. This study was motivated by the recent experiment [20] in which the frequencies of trapping potential of a stable BEC were changed [20]. One of the most striking observation in the experiment is that the condensate contains sheet-like structures rather than individual vortex cores in the dynamics by deforming the static trap [20]. By using the hydrodynamic forms of the GPE (1.3) in Thomas–Fermi regime, Cozzin and Stringari [18] tried to study this phenomena theoretically. But they did not find the sheet-like structures by changing the trap frequencies in their theoretical study. Here, we study this phenomena by directly simulating the GPE (1.3) using our new numerical method.

We take $d = 2$, $\beta_2 = 100$ and $\Omega = 0.99$ in (1.3). The initial data $\psi_0(\mathbf{x})$ in (1.4) is chosen as the ground state of (1.3) with $d = 2$, $\Omega = 0.99$, $\beta_2 = 100$ and $\gamma_x = \gamma_y = 1$, which is computed numerically by the normalized gradient

Table 3
Spatial discretization errors $\|\psi(t) - \psi^{(\Delta x, \Delta y, \Delta, \Delta z, t)}(t)\|_{l^2}$ at $t = 0.5$ in 3D

h	1	1/2	1/4
$\beta_3 = 20$	5.78E−2	1.27E−3	2.38E−8
$\beta_3 = 50$	0.1515	9.50E−3	2.45E−6
$\beta_3 = 100$	0.3075	3.88E−2	7.08E−5

Table 4
Temporal discretization errors $\|\psi(t) - \psi^{(\Delta x, \Delta y, \Delta z, \Delta t)}(t)\|_{l^2}$ at $t = 0.5$ in 3D

Δt	1/40	1/80	1/160	1/320	1/640
$\beta_3 = 20$	1.778E−4	4.435E−5	1.108E−5	2.767E−6	6.897E−7
$\beta_3 = 50$	6.266E−4	1.559E−4	3.892E−5	9.718E−6	2.422E−6
$\beta_3 = 100$	1.63E−3	4.0379E−4	1.0069E−4	2.5141E−5	6.265E−6

Fig. 1. Time evolution of the normalization $N(t) := N(\psi)(t)$, energy $E_{\beta,\Omega}(\psi)(t)$, angular momentum expectation $\langle L_z \rangle(t)$ (left column), and condensate widths $\delta_x(t)$, $\delta_y(t)$ and $\delta_r(t)$ (right column). Results in 2D for $\gamma_x = \gamma_y = 1$ (a and b), and $\gamma_x = 1$ and $\gamma_y = 2$ (c and d); and results in 3D for $\gamma_x = \gamma_y = \gamma_z = 1$ (e and f), and $\gamma_x = 1$, $\gamma_y = 2$ and $\gamma_z = 1.5$ (g and h).

flow proposed in [13]. In the ground state, there are about 61 vortices in the vortex lattice (cf. Fig. 2). We solve the problem on $\Omega_{\mathbf{x}} = [-24, 24] \times [-24, 24]$ with mesh size $\Delta x = \Delta y = 3/16$ and time step $\Delta t = 0.001$.

First, we study free expansion of the quantized vortex lattice. In general, the size of a stable vortex lattice in a BEC is too small to visualize it. In experiments, by removing the trap, i.e., letting the vortex lattice freely expands, one can obtain an enlarged vortex lattice so as to take a photo for it [20]. Of course, they hope the vortex structure does not change during the free expansion. Thus, theoretical study of free expansion is very helpful for experiments. We start with the stable BEC and remove the trapping at time $t = 0$, i.e. choosing $\gamma_x = \gamma_y = 0$ in (1.3). Similar numerical study was also carried out in [2] by a different numerical method with much less number of vortices in the lattice. Fig. 2 shows image plots of the density $|\psi(\mathbf{x}, t)|^2$ at different times for the free expansion of the vortex lattice. From the figure, we can see that when the trap is removed at $t = 0$, the vortex lattice will expand with time and the vortex structure as well as the rotational symmetry is kept during the expansion. This gives a numerical justification for the free expansion used in BEC experiments.

Next, we study dynamics of the quantized vortex lattice by changing the trap frequencies. We study six different cases: (I) $\gamma_x = 1$, $\gamma_y = 1.5$; (II) $\gamma_x = 1$, $\gamma_y = 0.75$; (III) $\gamma_x = 1.5$, $\gamma_y = 1$; (IV) $\gamma_x = 0.75$, $\gamma_y = 1$; (V) $\gamma_x = \sqrt{1.2}$, $\gamma_y = \sqrt{0.8}$; (VI) $\gamma_x = \sqrt{1.4}$, $\gamma_y = \sqrt{0.6}$. Similar numerical study was also carried out in [2] by a different method with much less number of vortices in the lattice. Fig. 3 shows image plots of the density $|\psi(\mathbf{x}, t)|^2$ at different times for cases I and II for changing frequencies in y-direction only. Fig. 4 shows similar results for cases III and IV for changing frequencies in x-direction only, and Fig. 5 for cases V and VI for changing frequencies in both x- and y-directions.

In Figs. 3–5, initially the condensate is assumed to be in its ground state which is a vortex lattice with about 61 vortices. From the numerical results presented here, when the trap frequencies are changed at $t = 0$, we find that: (i) cases I and II correspond to changing trap frequency in y-direction only. The condensate initially starts to contract (cf. (a) of Fig. 3) or expand (cf. (b) of Fig. 3) in y-direction since the trap frequency in y-direction is increasing or decreasing at $t = 0$. (ii) Cases III and IV correspond to changing trap frequency in x-direction only. Similar results are observed (cf. (a) and (b) of Fig. 4). (iii) Cases V and VI correspond to increasing and decreasing the trapping frequencies in x and y-directions by the same value, i.e., ϵ, respectively [18]. The condensate initially starts to contract and expand in x and y-directions, respectively (cf. Fig. 5).
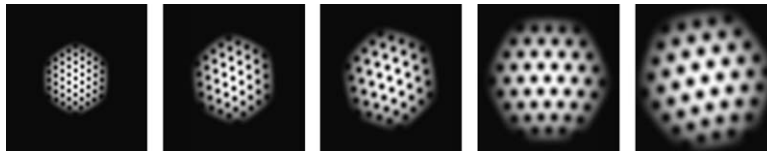

Fig. 2. Image plots of the density $|\psi(\mathbf{x}, t)|^2$ on $[-18, 18] \times [-18, 18]$ at different times $t = 0, 0.75, 1.5, 2.0$ and 2.75 (from left to right) for the free expansion of a quantized vortex lattice.
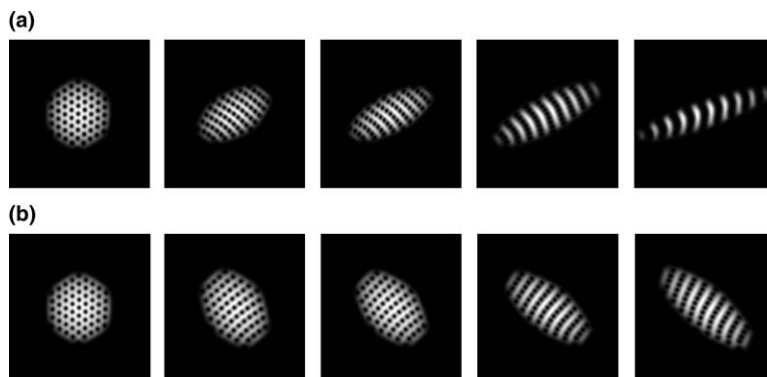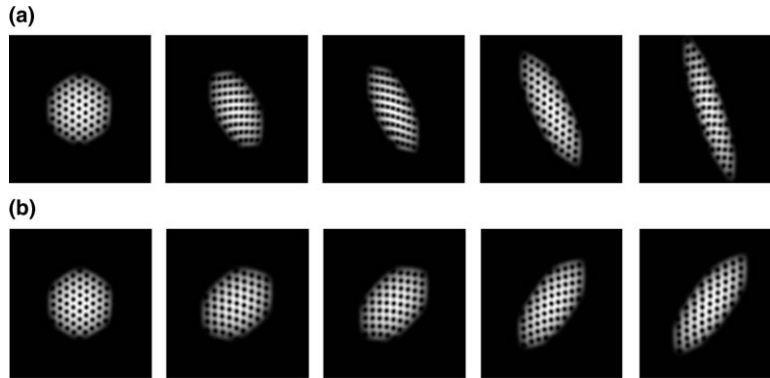
(a)

(b)

Fig. 3. Image plots of the density $|\psi(\mathbf{x}, t)|^2$ on $[-18, 18] \times [-18, 18]$ at different times $t = 0, 2.0, 4.0, 6.0,$ and 8.0 (from left to right) by changing frequency in y-direction only from $\gamma_y = 1$ to: (a) $\gamma_y = 1.5$; (b) $\gamma_y = 0.75$.

Fig. 4. Image plots of the density $|\psi(\mathbf{x}, t)|^2$ on $[-18, 18] \times [-18, 18]$ at different times $t = 0, 2.0, 4.0, 6.0,$ and 8.0 (from left to right) by changing frequency in x-direction only from $\gamma_x = 1$ to: (a) $\gamma_x = 1.5$; (b) $\gamma_x = 0.75$.

(iv) We numerically observed the remarkable sheet-like vortices in our numerical results (cf. Figs. 3 and 5). One can compare our numerical results in Figs. 3 and 5 with the experimental results, e.g. Fig. 4 in [20], and find very good qualitative agreement in sheet-like vortex lattice formation. Furthermore, we also found that when ϵ is bigger in cases V and VI, the sheet-like vortices appear earlier.

4.3. Generation of giant vortex in rotating BEC

In this subsection, we numerically generate a giant vortex in rotating BEC from its ground state by introducing a localized loss term [21]. This study was motivated by the recent experiment [21] and theoretical study
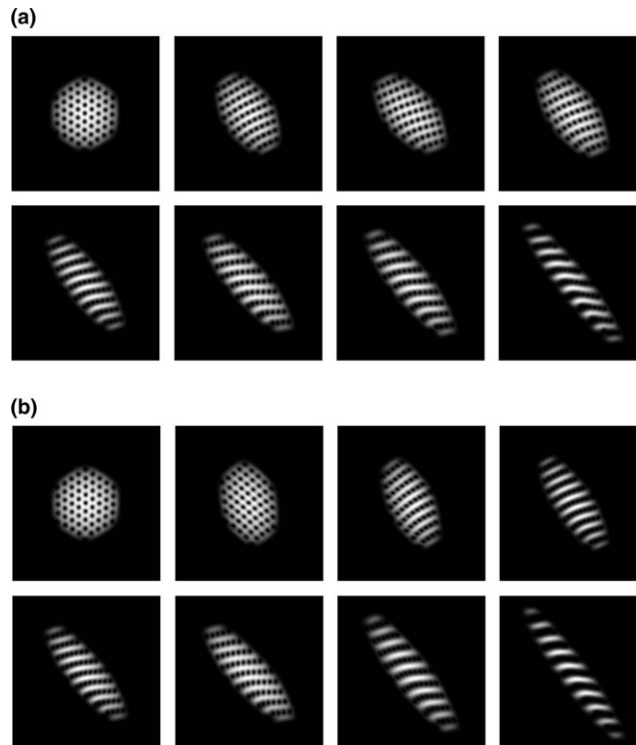

Fig. 5. Image plots of the density $|\psi(\mathbf{x}, t)|^2$ on $[-18, 18] \times [-18, 18]$ at different times by changing trapping frequencies from $\gamma_x = 1$, $\gamma_y = 1$ to $\gamma_x = \sqrt{1 + \epsilon}$, $\gamma_y = \sqrt{1.0 - \epsilon}$. (a) With $\epsilon = 0.2$ for times $t = 0, 2, 3, 4, 5, 6, 7$ and 8 (from left to right); (b) with $\epsilon = 0.4$ for times $t = 0, 1.0, 1.5, 2.0, 2.5, 3.0, 4.0$ and 4.5.

[36] in which the giant vortex formation arises as a dynamics effect. We take $d = 2$, $\beta_2 = 100$, $V_p(\mathbf{x}) \equiv 0$ and $\Omega = 0.99$ in (3.1). The initial data $\psi_0(\mathbf{x})$ in (3.3) is chosen as the ground state of (1.3) with $d = 2$, $\Omega = 0.99$, $\beta_2 = 100$ and $\gamma_x = \gamma_y = 1$, which is computed numerically by the normalized gradient flow proposed in [13]. The localized loss term in (3.1) is chosen as a Gaussian function of the form [36]

$$W(x, y) = w_0 \exp\left[-\frac{(x - x_0)^2 + (y - y_0)^2}{r_0^2}\right], \quad (x, y) \in \mathbb{R}^2, \tag{4.3}$$

where w_0, x_0, y_0 and r_0 are constants. We take $w_0 = 1$ and $r_0 = \sqrt{7}/2$ in (4.3) and solve the problem (3.1)–(3.3) on $\Omega_{\mathbf{x}} = [-24, 24] \times [-24, 24]$ with mesh size $\Delta x = \Delta y = 3/16$ and time step $\Delta t = 0.001$. Fig. 6 shows image plots of the density $|\psi(\mathbf{x}, t)|^2$ at different times for different values of (x_0, y_0).

From Fig. 6, we can see that the giant vortex lattice is generated due to the dynamic effect in a rotating BEC. The center of the giant vortex is the same as the center of the localized loss term and the size of the giant
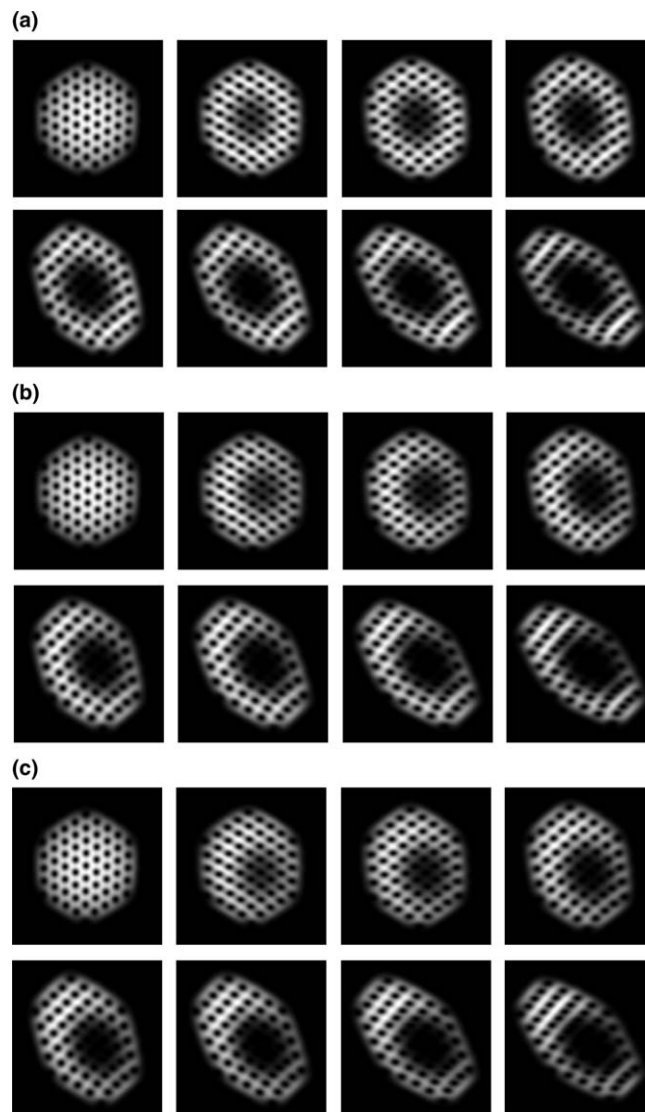

Fig. 6. Image plots of the density $|\psi(\mathbf{x}, t)|^2$ on $[-12, 12] \times [-12, 12]$ at different times $t = 0, 0.5, 0.75, 1.0, 1.25, 1.5, 1.75,$ and 2.0 (from left to right) with $w_0 = 1$ and $r_0 = \frac{\sqrt{7}}{2}$ in (4.3) for generating giant vortices. (a) $x_0 = 0$, $y_0 = 0$; (b) $x_0 = 1.5$, $y_0 = 0$; (c) $x_0 = 1.5$, $y_0 = 1$.

vortex depends on the values of r_0 and w_0. One can compare our numerical results in Fig. 6 with the experimental results, e.g., Fig. 1 in [21], and the theoretical study, e.g., Fig. 1 in [36], and find very good qualitative agreement in giant-vortex formation.

5. Conclusions

We have proposed a new time-spitting Fourier pseudospectral method for computing dynamics of rotating BEC based on an efficient approximation of GPE with an angular momentum rotation term. The new method is explicit, unconditionally stable, and of spectral accuracy in space and second-order accuracy in time. It is time reversible and time transverse invariant in the discretized level, just as the original GPE does, and conserves the total density in the discretized level. The efficient and accurate numerical method was applied to study dynamics of a quantized vortex lattice in rotating BEC. In the future, we plan to extend the idea for constructing the new numerical method for one component rotating BEC to multi-component rotating BEC and spinor dynamics in a rotational frame, and apply the method to study vortex line dynamics in rotating BEC in 3D.

Acknowledgments

Appendix A. Discretization in 2D

For each fixed y, the operator in Eq. (3.11) is in x-direction with constant coefficients and thus we can discretize it in x-direction by a Fourier pseudospectral method. Assume

$$\psi(x,y,t) = \sum_{p=-M/2}^{M/2-1} \hat{\psi}_p(y,t) \exp[i\mu_p(x-a)], \tag{A.1}$$

where $\mu_p = \frac{2p\pi}{b-a}$ and $\hat{\psi}_p(y,t)$ is the Fourier coefficient for the pth mode in x-direction. Plugging (A.1) into (3.11), noticing the orthogonality of the Fourier functions, we obtain for $-\frac{M}{2} \leqslant p \leqslant \frac{M}{2} - 1$ and $c \leqslant y \leqslant d$:

$$i\partial_t \hat{\psi}_p(y,t) = \left(\frac{1}{2}\mu_p^2 + \Omega y \mu_p\right) \hat{\psi}_p(y,t), \quad t_n \leqslant t \leqslant t_{n+1}. \tag{A.2}$$

The above linear ODE can be integrated in time *exactly* and we obtain

$$\hat{\psi}_p(y,t) = \exp\left[-i\left(\frac{1}{2}\mu_p^2 + \Omega y \mu_p\right)(t-t_n)\right] \hat{\psi}_p(y,t_n), \quad t_n \leqslant t \leqslant t_{n+1}. \tag{A.3}$$

Similarly, for each fixed x, the operator in Eq. (3.12) is in y-direction with constant coefficients and thus we can discretize it in y-direction by a Fourier pseudospectral method. Assume

$$\psi(x,y,t) = \sum_{q=-N/2}^{N/2-1} \hat{\psi}_q(x,t) \exp[i\lambda_q(y-c)], \tag{A.4}$$

where $\lambda_q = \frac{2q\pi}{d-c}$ and $\hat{\psi}_q(x,t)$ is the Fourier coefficient for the qth mode in y-direction. Plugging (A.4) into (3.12), noticing the orthogonality of the Fourier functions, we obtain for $-\frac{N}{2} \leqslant q \leqslant \frac{N}{2} - 1$ and $a \leqslant x \leqslant b$:

$$i\partial_t \hat{\psi}_q(x,t) = \left(\frac{1}{2}\lambda_q^2 - \Omega x \lambda_q\right) \hat{\psi}_q(x,t), \quad t_n \leqslant t \leqslant t_{n+1}. \tag{A.5}$$

Again the above linear ODE can be integrated in time *exactly* and we obtain

$$\hat{\psi}_q(x,t) = \exp\left[-\mathrm{i}\left(\frac{1}{2}\lambda_q^2 - \Omega x\lambda_q\right)(t - t_n)\right]\hat{\psi}_q(x, t_n), \quad t_n \leqslant t \leqslant t_{n+1}. \tag{A.6}$$

From time $t = t_n$ to $t = t_{n+1}$, we combine the splitting steps via the standard second-order Strang splitting [37,4,12]:

$$\psi_{jk}^{(1)} = \sum_{p=-M/2}^{M/2-1} \mathrm{e}^{-\mathrm{i}\Delta t(\mu_p^2 + 2\Omega y_k\mu_p)/4}\widehat{(\psi_k^n)}_p\mathrm{e}^{\mathrm{i}\mu_p(x_j-a)}, \quad 0 \leqslant j \leqslant M, \ 0 \leqslant k \leqslant N,$$

$$\psi_{jk}^{(2)} = \sum_{q=-N/2}^{N/2-1} \mathrm{e}^{-\mathrm{i}\Delta t(\lambda_q^2 - 2\Omega x_j\lambda_q)/4}\widehat{(\psi_j^{(1)})}_q\mathrm{e}^{\mathrm{i}\lambda_q(y_k-c)}, \quad 0 \leqslant k \leqslant N, \ 0 \leqslant j \leqslant M,$$

$$\psi_{jk}^{(3)} = \begin{cases} \mathrm{e}^{-\mathrm{i}\Delta t[V(x_j,y_k)+\beta_2|\psi_{jk}^{(2)}|^2]}\psi_{jk}^{(2)}, & W(x_j, y_k) = 0, \\ \dfrac{\psi_{jk}^{(2)}}{\mathrm{e}^{\Delta t W(x_j,y_k)}}\mathrm{e}^{-\mathrm{i}[\Delta t V(x_j,y_k)+\beta_2|\psi_{jk}^{(2)}|^2(1-\mathrm{e}^{-2\Delta t W(x_j,y_k)})/2W(x_j,y_k)]}, & W(x_j, y_k) > 0, \end{cases} \tag{A.7}$$

$$\psi_{jk}^{(4)} = \sum_{q=-N/2}^{N/2-1} \mathrm{e}^{-\mathrm{i}\Delta t(\lambda_q^2 - 2\Omega x_j\lambda_q)/4}\widehat{(\psi_j^{(3)})}_q\mathrm{e}^{\mathrm{i}\lambda_q(y_k-c)}, \quad 0 \leqslant k \leqslant N, \ 0 \leqslant j \leqslant M,$$

$$\psi_{jk}^{n+1} = \sum_{p=-M/2}^{M/2-1} \mathrm{e}^{-\mathrm{i}\Delta t(\mu_p^2 + 2\Omega y_k\mu_p)/4}\widehat{(\psi_k^{(4)})}_p\mathrm{e}^{\mathrm{i}\mu_p(x_j-a)}, \quad 0 \leqslant j \leqslant M, \ 0 \leqslant k \leqslant N,$$

where for each fixed k, $\widehat{(\psi_k^\alpha)}_p$ $(p = -M/2, \ldots, M/2 - 1)$ with α an index, the Fourier coefficients of the vector $\psi_k^\alpha = (\psi_{0k}^\alpha, \psi_{1k}^\alpha, \ldots, \psi_{(M-1)k}^\alpha)^\mathrm{T}$, are defined as

$$\widehat{(\psi_k^\alpha)}_p = \frac{1}{M}\sum_{j=0}^{M-1}\psi_{jk}^\alpha\mathrm{e}^{-\mathrm{i}\mu_p(x_j-a)}, \quad p = -\frac{M}{2}, \ldots, \frac{M}{2} - 1 \tag{A.8}$$

similarly, for each fixed j, $\widehat{(\psi_j^\alpha)}_q$ $(q = -N/1, \ldots, N/2 - 1)$, the Fourier coefficients of the vector $\psi_j^\alpha = (\psi_{j0}^\alpha, \psi_{j1}^\alpha, \ldots, \psi_{j(N-1)}^\alpha)^\mathrm{T}$, are defined as

$$\widehat{(\psi_j^\alpha)}_q = \frac{1}{N}\sum_{k=0}^{N-1}\psi_{jk}^\alpha\mathrm{e}^{-\mathrm{i}\lambda_q(y_k-c)}, \quad q = -\frac{N}{2}, \ldots, \frac{N}{2} - 1. \tag{A.9}$$

For the algorithm (A.7) presented in Appendix A, the total memory requirement is $\mathrm{O}(MN)$ and the total computational cost per time step is $\mathrm{O}(MN\ln(MN))$. The scheme is time reversible when $W(\mathbf{x}) \equiv 0$, just as it holds for the GPE (1.3), i.e. the scheme is unchanged if we interchange $n \leftrightarrow n + 1$ and $\Delta t \leftrightarrow -\Delta t$ in (A.7). Also, a main advantage of the numerical method is its time-transverse invariance when $W(\mathbf{x}) \equiv 0$, just as it holds for the GPE (1.3) itself. If a constant α is added to the external potential V, then the discrete wave functions ψ_{jk}^{n+1} obtained from (A.7) get multiplied by the phase factor $\mathrm{e}^{-\mathrm{i}\alpha(n+1)\Delta t}$, which leaves the discrete quadratic observable $|\psi_{jk}^{n+1}|^2$ unchanged. This property does not hold for the finite difference scheme [25,39], the leap-frog spectral method [41] and the efficient discretization proposed in [5] for GPE with an angular momentum term.

Appendix B. Discretization in 3D

For each fixed y, the operator in Eq. (3.13) is in x and z-directions with constant coefficients and thus we can discretize it in x and z-directions by a Fourier pseudospectral method. Similarly, for each fixed x, the operator in Eq. (3.14) is in y and z-directions with constant coefficients and thus we can discretize it in y and z-directions by a Fourier pseudospectral method. The discretizations of (3.13) and (3.14) are similar as those for (3.11) and (3.12), respectively, and they are omitted here. For simplicity and convenience of the reader, here we only present the algorithm for 3D GPE with an angular momentum rotation term (1.3) with $0 \leqslant j \leqslant M$, $0 \leqslant k \leqslant N$ and $0 \leqslant l \leqslant L$:

$$\psi_{jkl}^{(1)} = \sum_{p=-M/2}^{M/2-1} \sum_{s=-L/2}^{L/2-1} e^{-i\Delta t(2\mu_p^2+\gamma_s^2+4\Omega y_k \mu_p)/8} \; \widehat{(\psi_k^n)}_{ps} \, e^{i\mu_p(x_j-a)} \, e^{i\gamma_s(z_l-e)},$$

$$\psi_{jkl}^{(2)} = \sum_{q=-N/2}^{N/2-1} \sum_{s=-L/2}^{L/2-1} e^{-i\Delta t(2\lambda_q^2+\gamma_s^2-4\Omega x_j \lambda_q)/8} \; \widehat{(\psi_j^{(1)})}_{qs} \, e^{i\lambda_q(y_k-c)} \, e^{i\gamma_s(z_l-e)},$$

$$\psi_{jkl}^{(3)} = \begin{cases} e^{-i\Delta t[V(x_j,y_k,z_l)+\beta_3|\psi_{jkl}^{(2)}|^2]}\psi_{jkl}^{(2)}, & W(x_j,y_k,z_l) = 0, \\ \dfrac{\psi_{jkl}^{(2)}}{e^{\Delta t W(x_j,y_k,z_l)}} \exp[-i(\Delta t V(x_j,y_k,z_l) + \beta_3|\psi_{jkl}^{(2)}|^2(1-e^{-2\Delta t W(x_j,y_k,z_l)})/2W(x_j,y_k,z_l))], & W(x_j,y_k,z_l) > 0, \end{cases}$$

$$\psi_{jkl}^{(4)} = \sum_{q=-N/2}^{N/2-1} \sum_{s=-L/2}^{L/2-1} e^{-i\Delta t(2\lambda_q^2+\gamma_s^2-4\Omega x_j \lambda_q)/8} \; \widehat{(\psi_j^{(3)})}_{qs} e^{i\lambda_q(y_k-c)} e^{i\gamma_s(z_l-e)},$$

$$\psi_{jkl}^{n+1} = \sum_{p=-M/2}^{M/2-1} \sum_{s=-L/2}^{L/2-1} e^{-i\Delta t(2\mu_p^2+\gamma_s^2+4\Omega y_k \mu_p)/8} \; \widehat{(\psi_k^{(4)})}_{ps} e^{i\mu_p(x_j-a)} e^{i\gamma_s(z_l-e)}, \tag{B.1}$$

where for each fixed k, $\widehat{(\psi_k^\alpha)}_{ps}$ $(-M/2 \leqslant p \leqslant M/2-1, \; -L/2 \leqslant s \leqslant L/2-1)$ with α an index, the Fourier coefficients of the vector ψ_{jkl}^α $(0 \leqslant j < M, \; 0 \leqslant l < L)$, are defined as

$$\widehat{(\psi_k^\alpha)}_{ps} = \frac{1}{ML} \sum_{j=0}^{M-1} \sum_{l=0}^{L-1} \psi_{jkl}^\alpha e^{-i\mu_p(x_j-a)} e^{-i\gamma_s(z_l-e)}, \quad -\frac{M}{2} \leqslant p < \frac{M}{2}, \; -\frac{L}{2} \leqslant s < \frac{L}{2}$$

similarly, for each fixed j, $\widehat{(\psi_j^\alpha)}_{qs}$ $(-N/1 \leqslant q \leqslant N/2-1, \; -L/2 \leqslant s \leqslant L/2-1)$ with α an index, the Fourier coefficients of the vector ψ_{jkl}^α $(k=0,\ldots,N, \; l=0,\ldots,L)$, are defined as

$$\widehat{(\psi_j^\alpha)}_{qs} = \frac{1}{NL} \sum_{m=0}^{N-1} \sum_{l=0}^{L-1} \psi_{jkl}^\alpha e^{-i\lambda_q(y_k-c)} e^{-i\gamma_s(z_l-e)}, \quad -\frac{N}{2} \leqslant q < \frac{N}{2}, \; -\frac{L}{2} \leqslant s < \frac{L}{2}$$

with $\gamma_s = \frac{2\pi s}{f-e}$ for $s = -L/2,\ldots,L/2-1$.

For the discretization in 3D, the total memory requirement is O(MNL) and the total computational cost per time step is O($MNL \ln(MNL)$). Furthermore, the discretization is time reversible and time transverse invariant in the discretized level when $W(\mathbf{x}) \equiv 0$.

References

[1] J.R. Abo-Shaeer, C. Raman, J.M. Vogels, W. Ketterle, Observation of vortex lattices in Bose–Einstein condensates, Science 292 (2001) 476.

[2] S.K. Adhikari, P. Muruganandam, Effect of an impulsive force on vortices in a rotating Bose–Einstein condensate, Phys. Lett. A 301 (2002) 333–339.

[3] A. Aftalion, Q. Du, Vortices in a rotating Bose–Einstein condensate: critical angular velocities and energy diagrams in the Thomas–Fermi regime, Phys. Rev. A 64 (2001) 063603.

[4] W. Bao, Ground states and dynamics of multi-component Bose–Einstein condensates, Multiscale Modeling and Simulation 2 (2004) 210–236.

[5] W. Bao, Q. Du and Y. Zhang, Dynamics of rotating Bose–Einstein condensates and their efficient and accurate numerical computation, SIAM J. Appl. Math., to appear.

[6] W. Bao, D. Jaksch, An explicit unconditionally stable numerical method for solving damped nonlinear Schrodinger equations with a focusing nonlinearity, SIAM J. Numer. Anal. 41 (2003) 1406–1426.

[7] W. Bao, D. Jaksch, P.A. Markowich, Numerical solution of the Gross–Pitaevskii equation for Bose–Einstein condensation, J. Comput. Phys. 187 (2003) 318–342.

[8] W. Bao, D. Jaksch, P.A. Markowich, Three dimensional simulation of Jet formation in collapsing condensates, J. Phys. B 37 (2004) 329–343.

[9] W. Bao, S. Jin, P.A. Markowich, On time-splitting spectral approximations for the Schrödinger equation in the semiclassical regime, J. Comput. Phys. 175 (2002) 487–524.

[10] W. Bao, S. Jin, P.A. Markowich, Numerical study of time-splitting spectral discretizations of nonlinear Schrödinger equations in the semi-clasical regimes, SIAM J. Sci. Comput. 25 (2003) 27–64.

[11] W. Bao, Y. Zhang, Dynamics of the ground state and central vortex states in Bose–Einstein condensation, Math. Mod. Meth. Appl. Sci. 15 (2005) 1863–1896.
[12] W. Bao, J. Shen, A fourth-order time-splitting Laguerre–Hermite pseudo-spectral method for Bose–Einstein condensates, SIAM J. Sci. Comput. 26 (2005) 2010–2028.
[13] W. Bao, H. Wang, P.A. Markowich, Ground state, symmetric and central vortex state in rotating Bose–Einstein condensate, Commun. Math. Sci. 3 (2005) 57–88.
[14] Y. Castin, R. Dum, Bose–Einstein condensates with vortices in rotating traps, Eur. Phys. J. D 7 (1999) 399–412.
[15] M.M. Cerimele, M.L. Chiofalo, F. Pistella, S. Succi, M.P. Tosi, Numerical solution of the Gross–Pitaevskii equation using an explicit finite-difference scheme: an application to trapped Bose–Einstein condensates, Phys. Rev. E 62 (2000) 1382–1389.
[16] M.M. Cerimele, F. Pistella, S. Succi, Particle-inspired scheme for the Gross–Pitaevskii equation: an application to Bose–Einstein condensation, Comput. Phys. Commun. 129 (2000) 82–90.
[17] I. Coddington, P.C. Haljan, P. Engels, V. Schweikhard, S. Tung, E.A. Cornell, Experimental studies of equilibrium vortex properties in a Bose-condensed gas, Phys. Rev. A 70 (2004) 063607.
[18] M. Cozzini, S. Stringari, Macroscopic dynamics of a Bose–Einstein condensate containing a vortex lattice, Phys. Rev. A 67 (2003) 041602.
[19] F. Dalfovo, S. Giorgini, Theory of Bose–Einstein condensation in trapped gases, Rev. Mod. Phys. 71 (1999) 463.
[20] P. Engels, I. Coddington, P.C. Haljan, E.A. Cornell, Nonequilibrium effects of anisotropic compression applied to vortex lattices in Bose–Einstein condensates, Phys. Rev. Lett. 89 (2002) 100403.
[21] P. Engels, I. Coddington, V. Schweikhard, E.A. Cornell, Phys. Rev. Lett. 90 (2003) 170405.
[22] D.L. Feder, C.W. Clark, B.I. Schneider, Nucleation of vortex arrays in rotating anisotropic Bose–Einstein condensates, Phys. Rev. A 61 (1999) 011601.
[23] A.L. Fetter, A.A. Svidzinsky, Vortices in a trapped dilute Bose- Einstein condensate, J. Phys. Condens. Matter 13 (2001) R135-194.
[24] P.C. Haljan, I. Coddington, P. Engels, E.A. Cornell, Phys. Rev. Lett. 87 (2001) 210403.
[25] K. Kasamatsu, M. Tsubota, Nonlinear dynamics for vortex formation in a rotating Bose–Einstein condensate, Phys. Rev. A 67 (2003) 033610.
[26] A.E. Leanhardt, A. Görlitz, A.P. Chikkatur, D. Kielpinski, Y. Shin, D.E. Pritchard, W. Ketterle, Imprinting vortices in a Bose–Einstein condensate using topological phases, Phys. Rev. Lett. 89 (2002) 190403.
[27] A.E. Leanhardt, Y. Shin, D. Kielpinski, D.E. Pritchard, W. Ketterle, Coreless vortex formation in a spinor Bose–Einstein condensate, Phys. Rev. Lett. 90 (2003) 140403.
[28] C. Lobo, A. Sinatra, Y. Castin, Vortex lattice formation in Bose–Einstein condensates, Phys. Rev. Lett. 92 (2004) 020403.
[29] K.W. Madison, F. Chevy, W. Wohlleben, J. Dal-ibard, Vortex formation in a stirred Bose–Einstein condensate, Phys. Rev. Lett. 84 (2000) 806.
[30] M.R. Matthews, B.P. Anderson, P.C. Haljan, D.S. Hall, C.E. Wieman, E.A. Cornell, Vortices in a Bose–Einstein condensate, Phys. Rev. Lett. 83 (1999) 2498.
[31] A. Minguzzi, S. Succi, F. Toschi, M.P. Tosi, P. Vignolo, Numerical methods for atomic quantum gases with applications to Bose–Einstein condensates and to ultracold fermions, Phys. Rep. 395 (2004) 223–355.
[32] P. Muruganandam, S.K. Adhikari, Bose–Einstein condensation dynamics in three dimensions by pseudospectral and finite-difference methods, J. Phys. B 36 (2003) 2501–2513.
[33] M. Nakahara, T. Isoshima, K. Machida, S.-I. Ogawa, T. Ohmi, Physica B 17 (2000) 284–288.
[34] A.A. Penckwitt, R.J. Ballagh, Nucleation, growth, and stabilization of Bose–Einstein condensate vortex lattices, Phys. Rev. Lett. 89 (2002) (Article 260402).
[35] C. Raman, J.R. Abo-Shaeer, J.M. Vogels, K. Xu, W. Ketterle, Vortex nucleation in a stirred Bose–Einstein condensate, Phys. Rev. Lett. 87 (2001) 210402.
[36] T.P. Simula, A.A. Penckwitt, R.J. Ballagh, Giant vortex lattice deformation in rapidly rotating Bose–Einstein condensates, Phys. Rev. Lett. 92 (2004) (Article 060401).
[37] G. Strang, On the construction and comparison of difference schemes, SIAM J. Numer. Anal. 5 (1968) 505–517.
[38] M. Tsubota, K. Kasamatsu, M. Ueda, Vortex lattice formation in a rotating Bose–Einstein condensate, Phys. Rev. A 65 (2002) 023603.
[39] H. Wang, Numerical studies on the split-step finite difference method for nonlinear Schrödinger equations, Appl. Math. Comput. 170 (2005) 17–35.
[40] J.E. Williams, M.J. Hooand, Preparing topological states of a Bose–Einstein condensate, Nature 401 (1999) 568.
[41] Y. Zhang, W. Bao, Dynamics of the center of mass in rotating Bose–Einstein condensates, Appl. Numer. Math., to appear.